

Image registration and averaging of low laser power two-photon fluorescence images of mouse retina

Nathan S. Alexander,^{1,4} Grazyna Palczewska,² Patrycjusz Stremplewski,³ Maciej Wojtkowski,³ Timothy S. Kern,¹ and Krzysztof Palczewski^{1,2,5}

¹Department of Pharmacology, Cleveland Center for Membrane and Structural Biology, School of Medicine, Case Western Reserve University, Cleveland, OH 44106, USA

²Polgenix Inc., 11000 Cedar Ave, Cleveland, Ohio 44106, USA

³Faculty of Physics, Astronomy and Informatics, Institute of Physics, Nicolaus Copernicus University, 87-100 Torun, Poland

⁴nsa36@case.edu

⁵kxp65@case.edu

Abstract: Two-photon fluorescence microscopy (TPM) is now being used routinely to image live cells for extended periods deep within tissues, including the retina and other structures within the eye. However, very low laser power is a requirement to obtain TPM images of the retina safely. Unfortunately, a reduction in laser power also reduces the signal-to-noise ratio of collected images, making it difficult to visualize structural details. Here, image registration and averaging methods applied to TPM images of the eye in living animals (without the need for auxiliary hardware) demonstrate the structural information obtained with laser power down to 1 mW. Image registration provided between 1.4% and 13.0% improvement in image quality compared to averaging images without registrations when using a high-fluorescence template, and between 0.2% and 12.0% when employing the average of collected images as the template. Also, a diminishing return on image quality when more images were used to obtain the averaged image is shown. This work provides a foundation for obtaining informative TPM images with laser powers of 1 mW, compared to previous levels for imaging mice ranging between 6.3 mW [G. Palczewska, *Nat. Med.* **20**, 785 (2014)] and 9.5 mW [R. Sharma, *Biomed. Opt. Express* **4**, 1285 (2013)].

©2016 Optical Society of America

OCIS codes: (170.3880) Medical and biological imaging; (170.2520) Fluorescence microscopy; (100.2960) Image analysis.

References and links

1. G. Palczewska, T. Maeda, Y. Imanishi, W. Sun, Y. Chen, D. R. Williams, D. W. Piston, A. Maeda, and K. Palczewski, "Noninvasive multiphoton fluorescence microscopy resolves retinol and retinal condensation products in mouse eyes," *Nat. Med.* **16**(12), 1444–1449 (2010).
2. G. Palczewska, Z. Dong, M. Golczak, J. J. Hunter, D. R. Williams, N. S. Alexander, and K. Palczewski, "Noninvasive two-photon microscopy imaging of mouse retina and retinal pigment epithelium through the pupil of the eye," *Nat. Med.* **20**(7), 785–789 (2014).
3. V. E. Centonze and J. G. White, "Multiphoton Excitation Provides Optical Sections from Deeper within Scattering Specimens than Confocal Imaging," *Biophys. J.* **75**(4), 2015–2024 (1998).
4. P. Theer, M. T. Hasan, and W. Denk, "Two-photon imaging to a depth of 1000 microm in living brains by use of a Ti:Al₂O₃ regenerative amplifier," *Opt. Lett.* **28**(12), 1022–1024 (2003).
5. L. Rovati, S. Cattini, N. Zambelli, F. Viola, and G. Staurenghi, "In-vivo diffusing-wave-spectroscopy measurements of the ocular fundus," *Opt. Express* **15**(7), 4030–4038 (2007).
6. M. Hammer, A. Roggan, D. Schweitzer, and G. Müller, "Optical properties of ocular fundus tissues--an in vitro study using the double-integrating-sphere technique and inverse Monte Carlo simulation," *Phys. Med. Biol.* **40**(6), 963–978 (1995).
7. G. Palczewska, M. Golczak, D. R. Williams, J. J. Hunter, and K. Palczewski, "Endogenous fluorophores enable two-photon imaging of the primate eye," *Invest. Ophthalmol. Vis. Sci.* **55**(7), 4438–4447 (2014).

8. A. Vogel, C. Dlugos, R. Nuffer, and R. Birngruber, "Optical properties of human sclera, and their consequences for transscleral laser applications," *Lasers Surg. Med.* **11**(4), 331–340 (1991).
9. L. Kessel, J. H. Lundeman, K. Herbst, T. V. Andersen, and M. Larsen, "Age-related changes in the transmission properties of the human lens and their relevance to circadian entrainment," *J. Cataract Refract. Surg.* **36**(2), 308–312 (2010).
10. J. Dillon, L. Zheng, J. C. Merriam, and E. R. Gaillard, "Transmission spectra of light to the mammalian retina," *Photochem. Photobiol.* **71**(2), 225–229 (2000).
11. E. A. Boettner and J. R. Wolter, "Transmission of the Ocular Media," *Invest. Ophthalmol. Vis. Sci.* **1**, 776–783 (1962).
12. C. Xu and W. W. Webb, "Measurement of two-photon excitation cross sections of molecular fluorophores with data from 690 to 1050 nm," *J. Opt. Soc. Am. B* **13**(3), 481–491 (1996).
13. R. Sharma, L. Yin, Y. Geng, W. H. Merigan, G. Palczewska, K. Palczewski, D. R. Williams, and J. J. Hunter, "In vivo two-photon imaging of the mouse retina," *Biomed. Opt. Express* **4**(8), 1285–1293 (2013).
14. Q. Yang, J. Zhang, K. Nozato, K. Saito, D. R. Williams, A. Roorda, and E. A. Rossi, "Closed-loop optical stabilization and digital image registration in adaptive optics scanning light ophthalmoscopy," *Biomed. Opt. Express* **5**(9), 3174–3191 (2014).
15. B. D. Masella, D. R. Williams, W. S. Fischer, E. A. Rossi, and J. J. Hunter, "Long-Term Reduction in Infrared Autofluorescence Caused by Infrared Light Below the Maximum Permissible Exposure," *Invest. Ophthalmol. Vis. Sci.* **55**(6), 3929–3938 (2014).
16. J. I. W. Morgan, J. J. Hunter, B. Masella, R. Wolfe, D. C. Gray, W. H. Merigan, F. C. Delori, and D. R. Williams, "Light-induced retinal changes observed with high-resolution autofluorescence imaging of the retinal pigment epithelium," *Invest. Ophthalmol. Vis. Sci.* **49**(8), 3715–3729 (2008).
17. E. A. Rossi, M. Chung, A. Dubra, J. J. Hunter, W. H. Merigan, and D. R. Williams, "Imaging retinal mosaics in the living eye," *Eye (Lond.)* **25**(3), 301–308 (2011).
18. F. C. Delori, R. H. Webb, and D. H. Sliney, "Maximum permissible exposures for ocular safety (ANSI 2000), with emphasis on ophthalmic devices," *J. Opt. Soc. Am. A* **24**(5), 1250–1265 (2007).
19. L. R. Weisel, P. Xi, Y. Andegeko, V. V. Lovozoy, and M. Dantus, "Greater signal and contrast in two-photon microscopy with ultrashort pulses," *Proc. SPIE* **6860**, 68601O (2008).
20. R. D. Ferguson, Z. Zhong, D. X. Hammer, M. Mujat, A. H. Patel, C. Deng, W. Zou, and S. A. Burns, "Adaptive optics scanning laser ophthalmoscope with integrated wide-field retinal imaging and tracking," *J. Opt. Soc. Am. A* **27**, A265–A277 (2010).
21. J. J. Hunter, B. Masella, A. Dubra, R. Sharma, L. Yin, W. H. Merigan, G. Palczewska, K. Palczewski, and D. R. Williams, "Images of photoreceptors in living primate eyes using adaptive optics two-photon ophthalmoscopy," *Biomed. Opt. Express* **2**(1), 139–148 (2011).
22. R. Sharma, C. Schwarz, D. R. Williams, G. Palczewska, K. Palczewski, and J. J. Hunter, "In Vivo Two-Photon Fluorescence Kinetics of Primate Rods and Cones," *Invest. Ophthalmol. Vis. Sci.* **57**(2), 647–657 (2016).
23. Y. Geng, A. Dubra, L. Yin, W. H. Merigan, R. Sharma, R. T. Libby, and D. R. Williams, "Adaptive optics retinal imaging in the living mouse eye," *Biomed. Opt. Express* **3**(4), 715–734 (2012).
24. E. A. Rossi, P. Rangel-Fonseca, K. Parkins, W. Fischer, L. R. Latchney, M. A. Folwell, D. R. Williams, A. Dubra, and M. M. Chung, "In vivo imaging of retinal pigment epithelium cells in age related macular degeneration," *Biomed. Opt. Express* **4**(11), 2527–2539 (2013).
25. J. Zhang, Q. Yang, K. Saito, K. Nozato, D. R. Williams, and E. A. Rossi, "An adaptive optics imaging system designed for clinical use," *Biomed. Opt. Express* **6**(6), 2120–2137 (2015).
26. A. Dubra and Z. Harvey, "Registration of 2D Images from Fast Scanning Ophthalmic Instruments," in *Biomedical Image Registration: 4th International Workshop, WBIR 2010, Lübeck, Germany, July 11–13, 2010. Proceedings*, B. Fischer, B. M. Dawant, and C. Lorenz, eds. (Springer Berlin Heidelberg, Berlin, Heidelberg, 2010), pp. 60–71.
27. D. C. Gray, W. Merigan, J. I. Wolfing, B. P. Gee, J. Porter, A. Dubra, T. H. Twietmeyer, K. Ahamd, R. Tumber, F. Reinholz, and D. R. Williams, "In vivo fluorescence imaging of primate retinal ganglion cells and retinal pigment epithelial cells," *Opt. Express* **14**(16), 7144–7158 (2006).
28. D. J. Wahl, Y. Jian, S. Bonora, R. J. Zawadzki, and M. V. Sarunic, "Wavefront sensorless adaptive optics fluorescence biomicroscope for in vivo retinal imaging in mice," *Biomed. Opt. Express* **7**(1), 1–12 (2016).
29. D. S. Greenberg and J. N. D. Kerr, "Automated correction of fast motion artifacts for two-photon imaging of awake animals," *J. Neurosci. Methods* **176**(1), 1–15 (2009).
30. G. Kumar and S. T. L. Chung, "Characteristics of fixational eye movements in people with macular disease," *Invest. Ophthalmol. Vis. Sci.* **55**(8), 5125–5133 (2014).
31. F. Ratliff and L. A. Riggs, "Involuntary motions of the eye during monocular fixation," *J. Exp. Psychol.* **40**(6), 687–701 (1950).
32. S. Martinez-Conde, S. L. Macknik, and D. H. Hubel, "The role of fixational eye movements in visual perception," *Nat. Rev. Neurosci.* **5**(3), 229–240 (2004).
33. K. S. K. Wong, Y. Jian, M. Cua, S. Bonora, R. J. Zawadzki, and M. V. Sarunic, "In vivo imaging of human photoreceptor mosaic with wavefront sensorless adaptive optics optical coherence tomography," *Biomed. Opt. Express* **6**(2), 580–590 (2015).
34. Y. Matsumoto, "Ruby: A programmer's best friend" (2016), retrieved <https://www.ruby-lang.org/en/>.
35. T. Hunter, "RMagick Graphics Processing for Ruby and Ruby on Rails" (2016), retrieved 2016, <http://rmagick.rubyforge.org/>.
36. P. Strenplewski, K. Komar, K. Palczewski, M. Wojtkowski, and G. Palczewska, "Periscope for noninvasive two-photon imaging of murine retina in vivo," *Biomed. Opt. Express* **6**(9), 3352–3361 (2015).

37. B. D. Lucas and T. Kanade, "An iterative image registration technique with an application to stereo vision," in Proceedings of the 7th international joint conference on Artificial intelligence - **Volume 2**, (Morgan Kaufmann Publishers Inc., Vancouver, BC, Canada, 1981), pp. 674–679.
38. Y. Sun, S. Duthaler, and B. J. Nelson, "Autofocusing in computer microscopy: selecting the optimal focus algorithm," *Microsc. Res. Tech.* **65**(3), 139–149 (2004).
39. F. C. A. Groen, I. T. Young, and G. Ligthart, "A comparison of different focus functions for use in autofocus algorithms," *Cytometry* **6**(2), 81–91 (1985).
40. T. T. E. Yeo, S. H. Ong, Jayasooriah, and R. Sinniah, "Autofocusing for tissue microscopy," *Image Vis. Comput.* **11**(10), 629–639 (1993).
41. R. Sharma, D. R. Williams, G. Palczewska, K. Palczewski, and J. J. Hunter, "Two-Photon Autofluorescence Imaging Reveals Cellular Structures Throughout the Retina of the Living Primate Eye," *Invest. Ophthalmol. Vis. Sci.* **57**(2), 632–646 (2016).
42. I. J. T. Dobbins, "Image quality metrics for digital systems," in *Physics and Psychophysics*, R. L. V. Metter, J. Beutel, and H. L. Kundel, eds. (2000), pp. 161–222.
43. K. Carlsson and J. Philip, "Theoretical investigation of the signal-to-noise ratio for different fluorescence lifetime imaging techniques," *Proc. SPIE* **4622**, 70–78 (2002).
44. L. T. Schelhas, J. C. Shane, and M. Dantus, "Advantages of ultrashort phase-shaped pulses for selective two-photon activation and biomedical imaging," *Nanomedicine (Lond.)* **2**(3), 177–181 (2006).
45. A. Doerr, "Single-particle cryo-electron microscopy," *Nat. Methods* **13**(1), 23 (2015).
46. D. W. Piston, "Imaging living cells and tissues by two-photon excitation microscopy," *Trends Cell Biol.* **9**(2), 66–69 (1999).
47. D. Pestov, Y. Andegeko, V. V. Lozovoy, and M. Dantus, "Photobleaching and photoenhancement of endogenous fluorescence observed in two-photon microscopy with broadband laser sources," *J. Opt.* **12**, 8 (2010).
48. A. W. Stitt, T. M. Curtis, M. Chen, R. J. Medina, G. J. McKay, A. Jenkins, T. A. Gardiner, T. J. Lyons, H. P. Hammes, R. Simó, and N. Lois, "The progress in understanding and treatment of diabetic retinopathy," *Prog. Retin. Eye Res.* **51**, 156–186 (2016).
49. N. M. Bressler, S. B. Bressler, and S. L. Fine, "Age-related macular degeneration," *Surv. Ophthalmol.* **32**(6), 375–413 (1988).
50. H. Liu, J. Tang, Y. Du, C. A. Lee, M. Golczak, A. Muthusamy, D. A. Antonetti, A. A. Veenstra, J. Amengual, J. von Lintig, K. Palczewski, and T. S. Kern, "Retinylamine Benefits Early Diabetic Retinopathy in Mice," *J. Biol. Chem.* **290**(35), 21568–21579 (2015).
51. L. Yin, Y. Geng, F. Osakada, R. Sharma, A. H. Cetin, E. M. Callaway, D. R. Williams, and W. H. Merigan, "Imaging light responses of retinal ganglion cells in the living mouse eye," *J. Neurophysiol.* **109**(9), 2415–2421 (2013).

Abbreviations

TPM, two-photon fluorescence microscopy; NV, normalized variance; RPE, retinal pigmented epithelium; SNR, signal-to-noise ratio; MPE, maximum permissible exposure

1. Introduction

Two-photon fluorescence microscopy (TPM) is a powerful tool for imaging and diagnosing the health of the retina [1, 2]. In TPM a fluorescent signal is induced by the simultaneous absorption of two photons, enabling the use of wavelengths twice as long as would be required to induce single photon fluorescence. The longer wavelengths associated with two-photon imaging penetrate deeper into tissue than single photon fluorescence allows [3]. In two-photon imaging the fundamental imaging depth limit is at such a distance within a tissue where further increases in the excitation power do not improve imaging contrast. This loss of contrast deep within thick absorbing or scattering samples occurs because signaling from fluorophores located within the focal volume is overwhelmed by that from fluorophores located closer to sample surface and excited by scattered light [4]. Using photon transport mean-free-path length (L) in the retina for 750 nm light at 1.2 mm ($L = 0.27$ mm at 400 nm) based on previous reports of bovine retina [5, 6], the estimated maximal imaging depth is 2.4 mm - more than enough to penetrate the mouse retina. Taking into account dramatically shorter mean free paths in the RPE and choroid, the theoretical maximum depth is 0.44 mm, still sufficient to image mouse retina and RPE. This long penetration depth previously allowed collection of two-photon images of the RPE created by endogenous fluorophores [7].

The two-photon effect also is required to non-invasively induce fluorescence of endogenous fluorophores in the retina through the pupil, because the human cornea [8] and lens [9, 10] block shorter wavelengths of light [11] needed to excite such fluorophores by single photon absorption. Moreover, because of the time and spatial constraints required for

two photon-induced fluorescence, the signal is confined to the focal plane, reducing fluorescence from unwanted depths. However, small two-photon absorption cross-sections [12] necessitate a large photon flux to generate an imaging signal, which can result in tissue alteration. Moreover, tissue movements during live animal imaging reduces the efficacy of signal averaging and obstruct identification of biological structures [13, 14].

Obtaining TPM images with low laser power is critical to its safe application for clinical retinal imaging [13, 15–18]. Previously reported images of the RPE in live animals were obtained with 6.3 mW stimulation [2]. Even with advances in hardware to improve TPM efficiency, e.g. use of ultra-fast pulsed lasers [19], complementary software techniques will be required to reduce radiant exposure and improve the signal to noise ratio. Signal averaging of collected images can greatly improve their clarity. However, to apply averaging to TPM images, several questions must be answered. These include whether successful image registration can be obtained under noisy conditions, and how low a laser power can be used.

Image registration can permit a series of images to be averaged and bring features into alignment, even when local and non-linear perturbations occur between registered images [20]. Previous two-photon fluorescence studies of the retina *in vivo* utilized between 5000 and 21600 images for averaging [13, 21, 22] with laser powers between 2.6 mW and 14 mW. Many single-photon studies and all previous two-photon imaging studies of *in vivo* retina [13, 14, 21–25] employed a common registration method [26]. Briefly, this method maximizes the cross-correlation between images utilizing fast Fourier transform calculations over thin horizontal slices of image frames. But, the inability to register in the presence of torsional or rotational distortions is a limitation of this method [14, 25]. Moreover, this method also mandates the use of a template image on which subsequently collected frames can be aligned, a need commonly achieved using auxiliary reflectance imaging [21–25, 27, 28]. An alternative registration algorithm is derived from two-photon fluorescence neuronal imaging [29]. This method is generally applicable but was specifically designed for two-photon fluorescence imaging. It makes no assumptions about the type of motion that needs correction, so it even can handle rotational motion and was demonstrated to handle 10 μm motions [29].

Multiple types of motion of varying frequency and magnitude can affect images collected *in vivo*. During *in vivo* single-photon fluorescence imaging of human photoreceptors, a root mean square displacement from the template image of 26.9 μm was obtained [14]. The median rate of microsaccades in humans with and without macular disease are 2.48 and 1.49 per second [30]. The median amplitude of microsaccades is 52.96 arc min and 14.96 arc min for diseased and healthy subjects, respectively [30]. Microsaccades occur erratically every 0.2 up to 4.0 seconds [31] with a range of amplitudes, 2.2 to 25.8 arc min in healthy subjects [31, 32]. The median amplitude of slow drifts is 7.64 for healthy subjects [30]. Drift amplitudes range from 1.0 to 5.0 arc min, with between 2 and 5 per second. Tremors occur with a frequency of approximately 70 Hz [31, 32]. The tremor median amplitude is 17.5 arc sec [31], roughly the diameter of a human foveal cone [32] at 4–5 μm [20, 33]. Eye movement during *in vivo* imaging of anesthetized mouse retina is minimal whereas respiration creates the most movement [2]. Displacements from this respiration rate typically fall within 10 μm [29], with breathing occurring 145 times per minute [2]. The result of all these motions is that, without registration, biological structures are not discernible in the averaged image [13,20].

We hypothesized that TPM imaging data collected with low laser powers contains sufficient information to distinguish RPE cells. Therefore, TPM image data sets of RPE were collected with laser powers near-to those previously reported and below - down to 1mW. We show the effect of image averaging and registration on these data sets as well as images of retina capillaries injected with fluorescent dye. RPE cells are visible in images collected with 1 mW of laser power. Lastly, the decreasing benefit of adding additional images to the average image is demonstrated.

2. Methods

2.1 Implementation

The Ruby programming language [34] was used to implement our described image processing techniques. The software is available upon request. Additional libraries included the RMagick library for reading and writing images [35].

2.2 Mice for RPE image acquisition

RPE65^{-/-} mice were generated and genotyped as previously described [36]. Mice were housed in the animal facility at the School of Medicine, Case Western Reserve University, where they were maintained on a normal mouse chow diet in a 12 h light (~10 lux)/12 h dark cyclic environment. All animal procedures and experiments were approved by the Case Western Reserve University Animal Care Committee and conformed to both the recommendations of the American Veterinary Medical Association Panel on Euthanasia and the Association for Research in Vision and Ophthalmology. RPE65^{-/-} mice used in this study were 2–3 months old.

2.3 Mice for retinal capillary imaging

C57BL/6J pigmented (WT) mice were purchased from The Jackson Laboratory (Bar Harbor, Maine). In a subset of animals, diabetes was induced in 2 month old mice by five sequential daily intraperitoneal injections of a freshly prepared solution of streptozotocin in citrate buffer (pH 4.5) at 60 mg/kg of body weight. Before imaging, mice were injected with FITC-bovine serum albumin (BSA) into their tail veins. All mice were housed, and all regulatory requirements were satisfied as described above. WT mice used in this study were 4–6 months old.

2.4 Imaging by TPM

Before imaging, mice were anesthetized with an intraperitoneal injection of a solution consisting of ketamine (16.5 mg/mL) and xylazine (1.65 mg/mL) diluted in sterile water at a dose of 0.008 – 0.012 μ L/g body weight. Mice were located on a heated mechanical stage for imaging. Corneal lubrication was maintained with a thin layer of GenTeal gel (Novartis, NJ) squeezed between the cornea and a contact lens with zero refractive power. TPM images of the RPE in RPE65^{-/-} mice were collected as previously described [36] using 750 nm excitation beam. Laser-powers for RPE image acquisition experiments were 6.2 mW, 3.2 mW, 2.1 mW, 1.5 mW, and 1.0 mW. At each laser power, 150 images were collected. For RPE images, in addition to the 150 images collected for each laser power, an “ideal” template was collected for each of the five image sets using 31 mW of laser power (Fig. 9).

Retinal capillaries in C57BL/6J mice were imaged with 800 nm excitation light, 20–60 min after injection with FITC-BSA and application of a contact lens with a flat front, as noted previously [2]. Images of retinal capillaries were collected with a laser-power of 5 mW. Based on previous studies [1, 2], 5 mW was expected to provide strong fluorescence without damaging the retina, making capillaries visible in images. The purpose is to be able to demonstrate improvement in imaging capillary detail, which is important for evaluating progress in diabetic retinopathy. The number of images collected for each of the four series was 10, 5, 20, and 40. Obtaining differing number of images is due to the nature of *in vivo* imaging and is common in such imaging studies [14, 21–25, 27]. Each of the nine reported imaging series (five image series of RPE collected at different laser powers and four image series of retina capillaries) was derived from a single mouse, and each referred-to averaged image was derived from one of the nine image series. The time to obtain one imaging frame was 1.2 seconds. Images were collected at a resolution of 512x512 pixels, with a scale of 1.9 μ m per pixel.

2.5 Image registration

The image registration method used for all image registration tasks is described in detail by Greenburg et al. [29], based on the well-known method of Lucas and Kanade [37]. The protocol for image registration was as follows (Fig. 1). First, the image of interest, I , and template, T , to which I will be registered were smoothed, as previously described [14]. Smoothing was accomplished by setting each pixel to the average of all pixels not more than two rows or columns away from the current pixel. Second, I and T were globally translated by Fourier transform based rigid alignment, which maximizes the correlation between images. This reduces the burden on the subsequent non-rigid iterative registration step [14, 20]. Third, the number of support points defines the resolution at which different regions of the image can move independently of one another and the number of parameters being optimized. Here, the number of support points was set to the number of pixel rows in the images, similar to previous work [29]. Iterative image registration optimized the correlation between I and T . After the non-rigid registration in step three, the entire protocol was repeated for a second round, using the alignment results of the first round. The second round was performed without smoothing of T or I . Smoothing was performed in the first round to bring the major features into alignment so the second round could bring the details into alignment without smoothing. After registration, the images were averaged together by calculating the average intensity for each pixel over all the images.

A template must be defined to which the images will be aligned. Three templates were explored here. For images of RPE, an “ideal” template was collected with high-laser power. For images of retina vasculature, a manually selected single image from the set of images served as a template. The third template originated from averaging the set of images without registration, and using that averaged image as the template for registration. To generate the average template for an image series, all images from the series were included in the average.

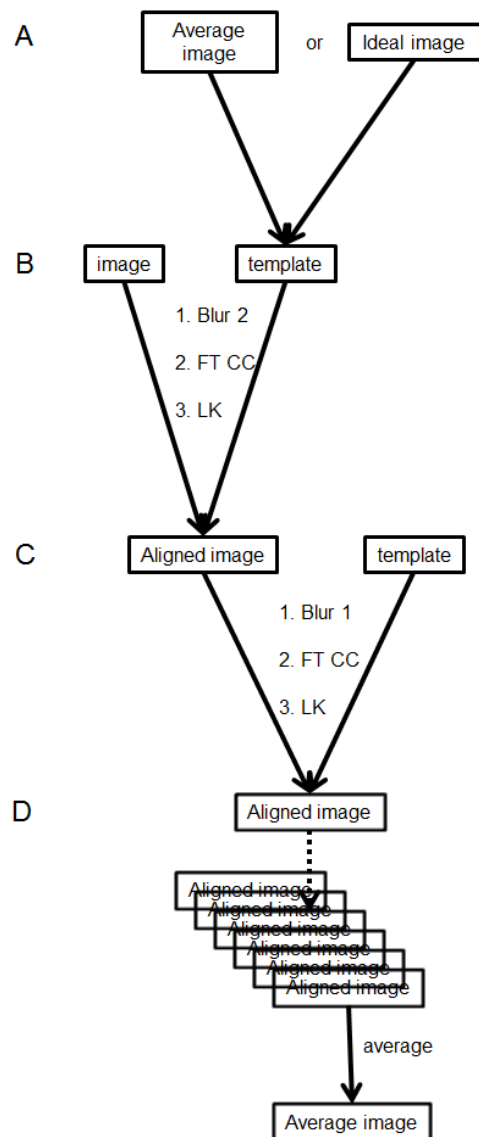


Fig. 1. Flow chart of alignment procedure. A) A template image is obtained either from averaging all images in a series together without alignment, or a highly fluorescent image. B) The image of interest is aligned to the template image in a three step procedure. 1) Both the image and the template are blurred by averaging a two pixel radius around each pixel. 2) The orientation of the image maximizing its cross correlation with the template is determined using Fourier transform- based alignment. 3) The non-rigid registration algorithm based on Lukas and Kanade is used to register the image to the template. D) Steps B and C are repeated for every image in an imaging series producing a set of aligned images. These images are then averaged together to produce the average image.

2.6 Image quality

Image quality was quantified with the normalized variance (NV) quality measure, which has been shown to be a well-behaved measure of image quality even under noisy conditions, with a larger NV indicating better quality images [38–40]. In addition, NV was demonstrated to

select better quality images during optimization of wavefront sensor free adaptive optics for *in vivo* two-photon fluorescence retina imaging [2]. NV is calculated by Eq. (1):

$$NV = \frac{1}{(HW\mu^2)} \sum_H \sum_w \left((i(w,h) - \mu)^2 \right), \quad (1)$$

where H is the height of the image, W is the width of the image, μ is the average image intensity, and $i(w,h)$ is the intensity of the pixel at location (w, h) .

To complement the NV values, signal-to-noise ratios (SNRs) also were calculated as a metric for the images [41]. For fluorescence microscopy, and assuming shot noise limited detection, the SNR can be calculated by Eq. (2):

$$SNR = \frac{N}{\sqrt{N}}, \quad (2)$$

where N is the number of detected photons [42, 43]. Here, we used the measured pixel intensity values as N , because these values are directly related to the number of detected photons in our experiments. A value of 256 indicates saturation.

2.7 Image brightening

The present main goal for collecting two-photon fluorescence images of the retina is to distinguish biological structures. A common practice is to increase image pixel intensities so that the biological structures can be better visualized [19, 44]. Here, images of RPE were brightened by scaling all the intensities from 0 to max pixel intensity.

2.8 Estimation of significant changes in NV

For each of the nine total data series of RPE and vasculature, a single average-image was obtained for each registration condition (no registration; using an “average” template; using a single-image template) for which the NV was calculated. Having single resulting images creates a challenge for determining when changes in NV are statistically significant. Visual examination is one method that could be used for comparing images to see if there is an obvious qualitative improvement in image quality. However, a quantitative estimate for the standard deviation around the NV values would be even more desirable. Therefore, we calculated a rough estimate of the standard deviation for the NV values of the averaged-images, by assuming the standard deviation in NV values for average images is similar to the standard deviation in NV values for single images. First, the NV value for all images in a data series was calculated. Second, the means and standard deviations of the NV values in that data series were determined, and then those two values were used to obtain the ratio of the standard deviation to the mean for that data set. This ratio was calculated for all data series, and then the average ratio was calculated. This number was multiplied by 100 to determine the average percent the standard deviation was of the mean. This averaged ratio of standard deviation to mean was 1.8% (standard deviation 0.6), in good agreement with a previously published value of 1% for a standard deviation of the NV for sequentially collected images [39]. Based on this result, we suggest NV changes are significant when they are 1.8% or greater of the initial NV value (bold values, Tables 1 and 2).

3. Results

3.1 Single and average images without registration

Images of RPE were collected with laser powers at 6.2 mW, 3.2 mW, 2.1 mW, 1.5 mW, and 1.0 mW (Fig. 2, Fig. 3). As the laser power decreased, RPE cells became indistinguishable from noise in single images (Fig. 2(A), 2(C), 2(E); Fig. 3(A), 3(C)). For each laser power, 150 images were collected. Upon averaging these 150 images, even without any registration, the RPE cells could be distinguished (Fig. 2(B), 2(D), 2(F); Fig. 3(B), 3(D)).

Images of the retina vasculature were collected with TPM after injecting fluorescent dye (Fig. 4). Due to the highly fluorescent dye used, all of these images displayed strong vascular contrast. With the increased fluorescence and fine capillary structures, compared to the RPE images, the blurring of structures after averaging the images without registration is evident (Fig. 4(B), 4(D), 4(F), 4(H)).

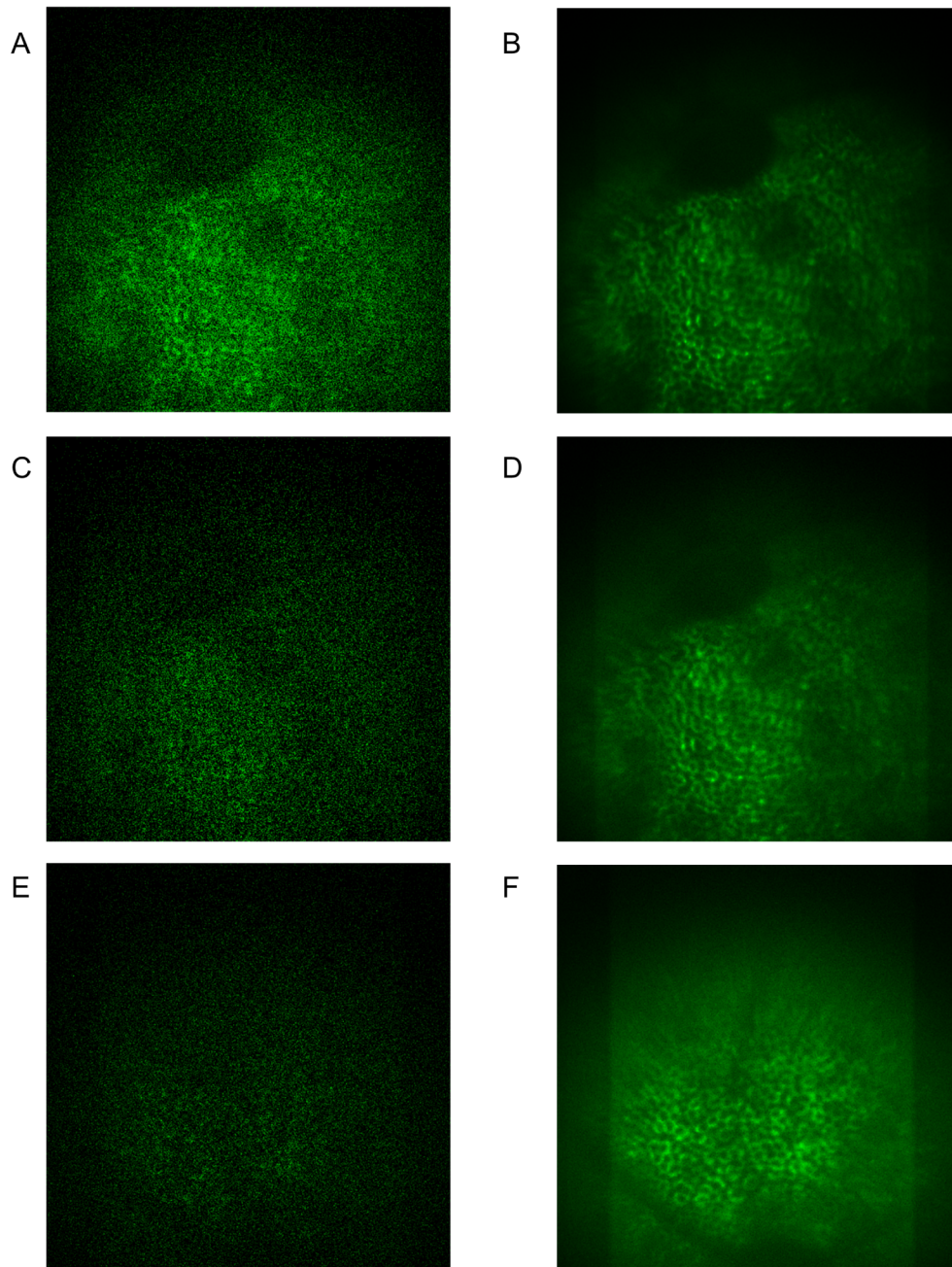


Fig. 2. Single images collected with laser powers of A) 6.2 mW, C) 3.2 mW, E) 2.1 mW. On the right are images resulting from averaging 150 images collected with laser powers of B) 6.2 mW C) 3.2 mW, F) 2.1 mW. To reveal image content better, images were brightened as described in Methods.

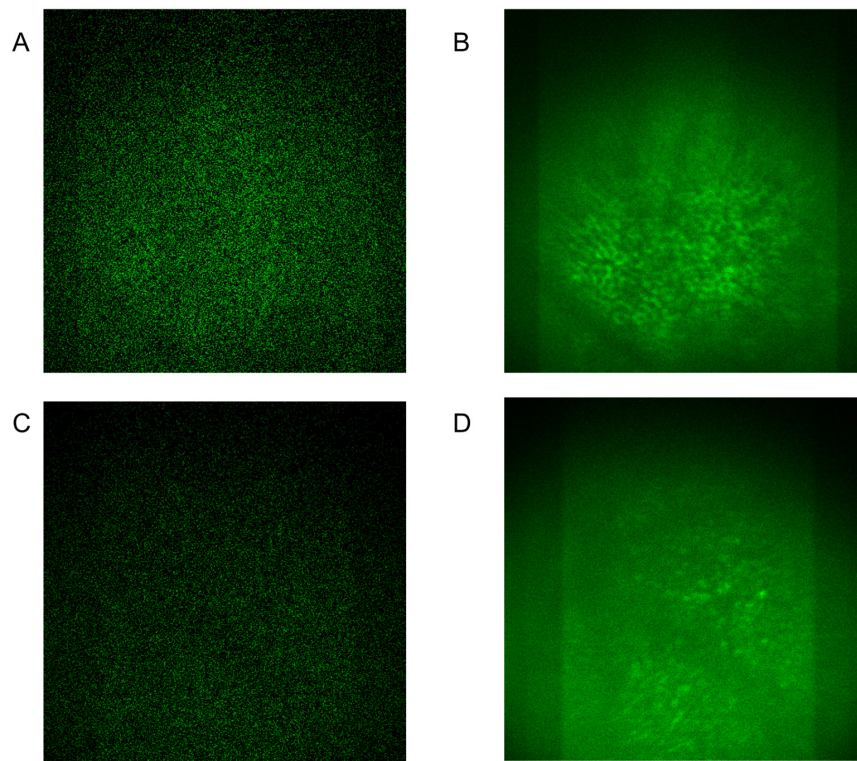


Fig. 3. Single images collected with laser powers of A) 1.5 mW, C) 1.0 mW. On the right are images resulting from averaging 150 images collected with laser powers of B) 1.5 mW D) 1.0 mW. To reveal image content better, images were brightened as described in Methods.

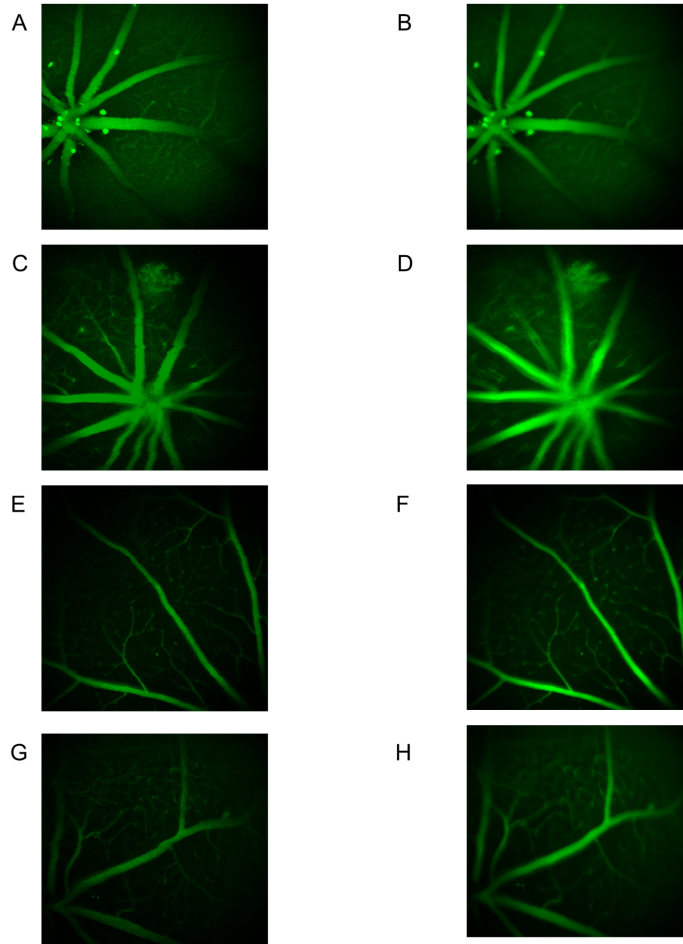


Fig. 4. Images collected of retina vasculature. A), C), E), G) Single images. Average of B) 9, D) 5, F) 20, H) 40 images without any registration. All images were collected at 5 mW of laser power.

3.2 Registration to an average image template and registration to a single-image template

An “average” template was created by averaging the 150 images together, without any registration (Fig. 2(B), 2(D), 2(F); Fig. 3(B), 3(D)). The 150 images were then averaged after being registered to the “average” template (Fig. 5(A), 5(C), 5(E); Fig. 6(A), 6(C)) and the “ideal” template collected with 31 mW of laser power (Fig. 5(B), 5(D), 5(F); Fig. 6(B), 6(D)). Comparison of the average image derived from each of the two templates showed little qualitative difference in the resulting averaged image (Fig. 5, Fig. 6). The decrease in NV due to using the “average” template compared to the high-power template was 3% or less across all power levels tested (Table 1). Comparing the average image generated without registration to the average image generated when each of the two templates were used shows that there was an improvement in NV of between 0.2% and 1.9% when the “average” template was used for registration. When the “ideal” template was used for registration, an improvement of between 1.4% and 3.4% was seen, compared to when no registration was performed before averaging (Table 1).

For vasculature, images were aligned either by using an “average” template, as described above, or a manually selected single template (Fig. 7). Comparing NV for the two sets of average images (Table 2) revealed that using the unregistered average as the template for

registration resulted in less than a 3.4% decrease in image quality, in the worst case, compared to using a template based on a single image. For two of the image series, using the “average” template resulted in a 1% improvement in the NV value. Comparing the average image generated without registration to the average image generated when each of the two templates was used shows that there was an improvement in NV of between 4.6% and 12.0% when the “average” template was used for registration. When the single-image template was used for registration, an improvement of between 3.0% and 13.0% was seen, compared to when no registration was performed before averaging (Table 2).

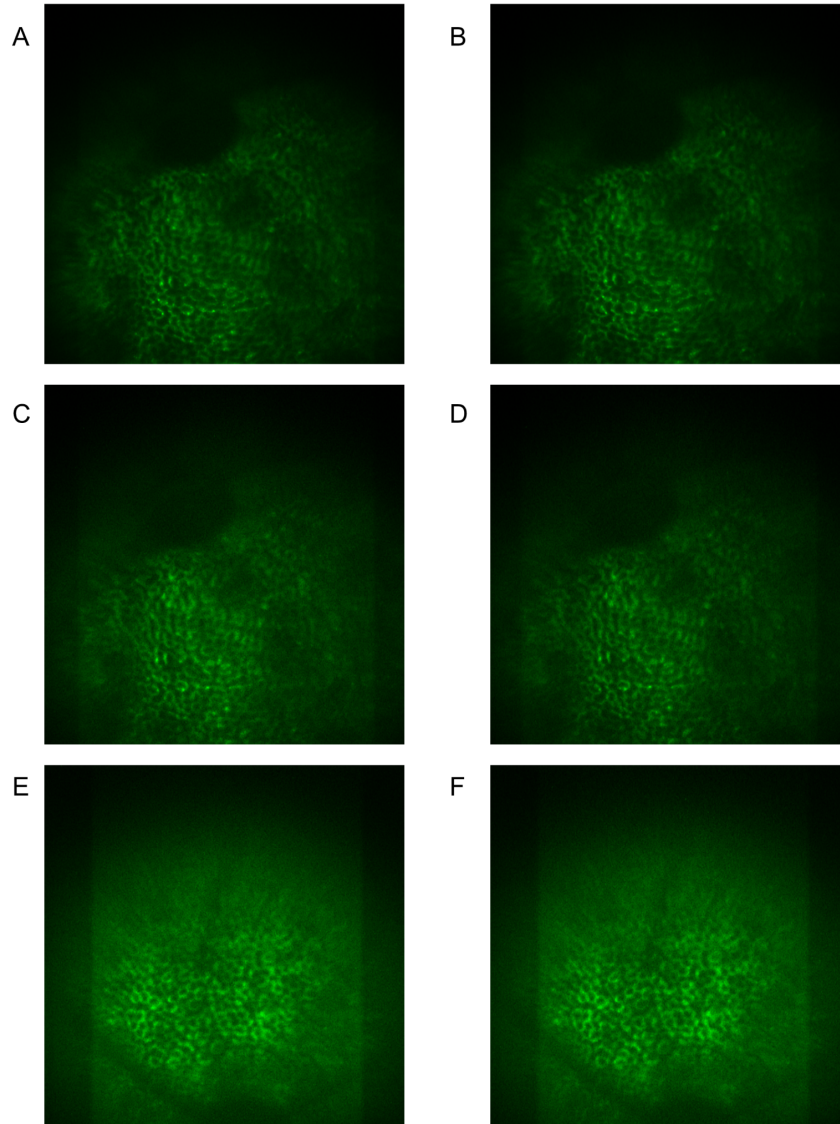


Fig. 5. Ideal versus average template comparison for images of RPE. Comparison of registration to an unregistered average image (A, C, E) versus image registration to an ideal template image (B, D, F). Laser powers used to collect 150 images for averaging were 6.2 mW (A), 3.2 mW (C), 2.1 mW (E). To reveal image content better, images were brightened as described in Methods. Ideal template images used for registration in (B, D, F) were collected with laser power of 31mW.

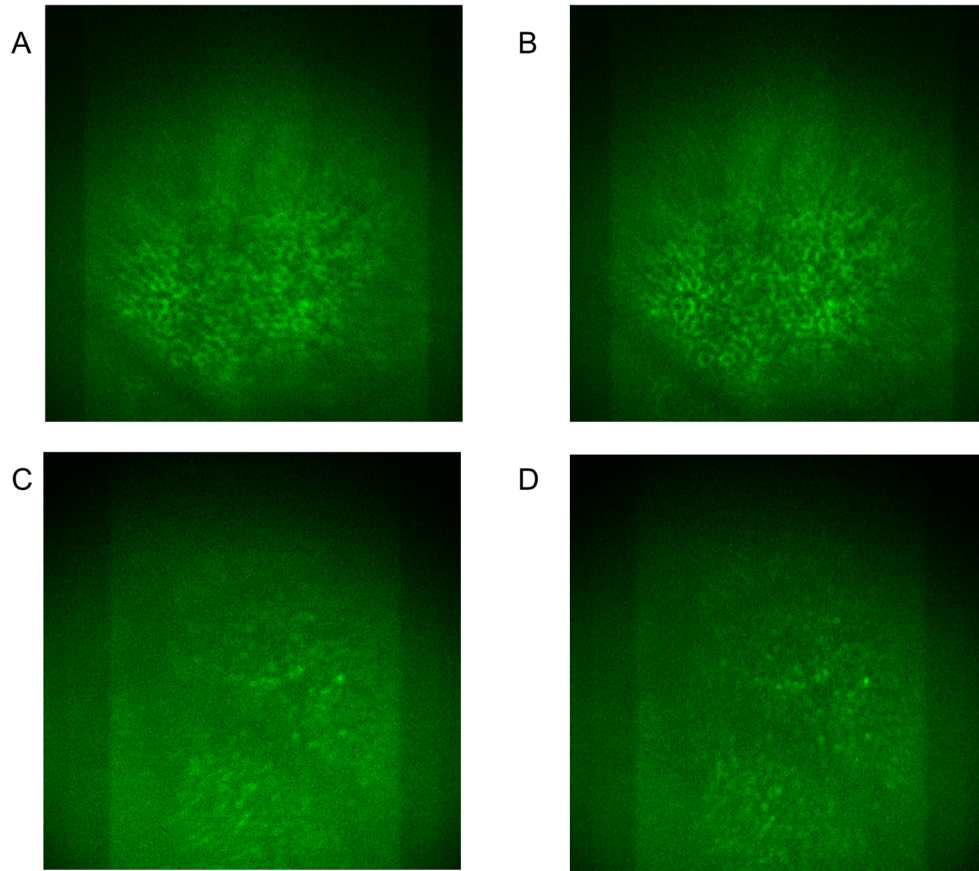


Fig. 6. Ideal versus average template comparison for images of RPE. Comparison of registration to an unregistered average image (A, C) versus image registration to an ideal template image (B, D). Ideal template images used for registration in (B, D) were collected with laser power of 31mW. Laser powers used to collect 150 images for averaging were 1.5 mW (A, B), and 1.0 mW (C, D). To reveal image content better, brightness of images was increased as described in Methods.

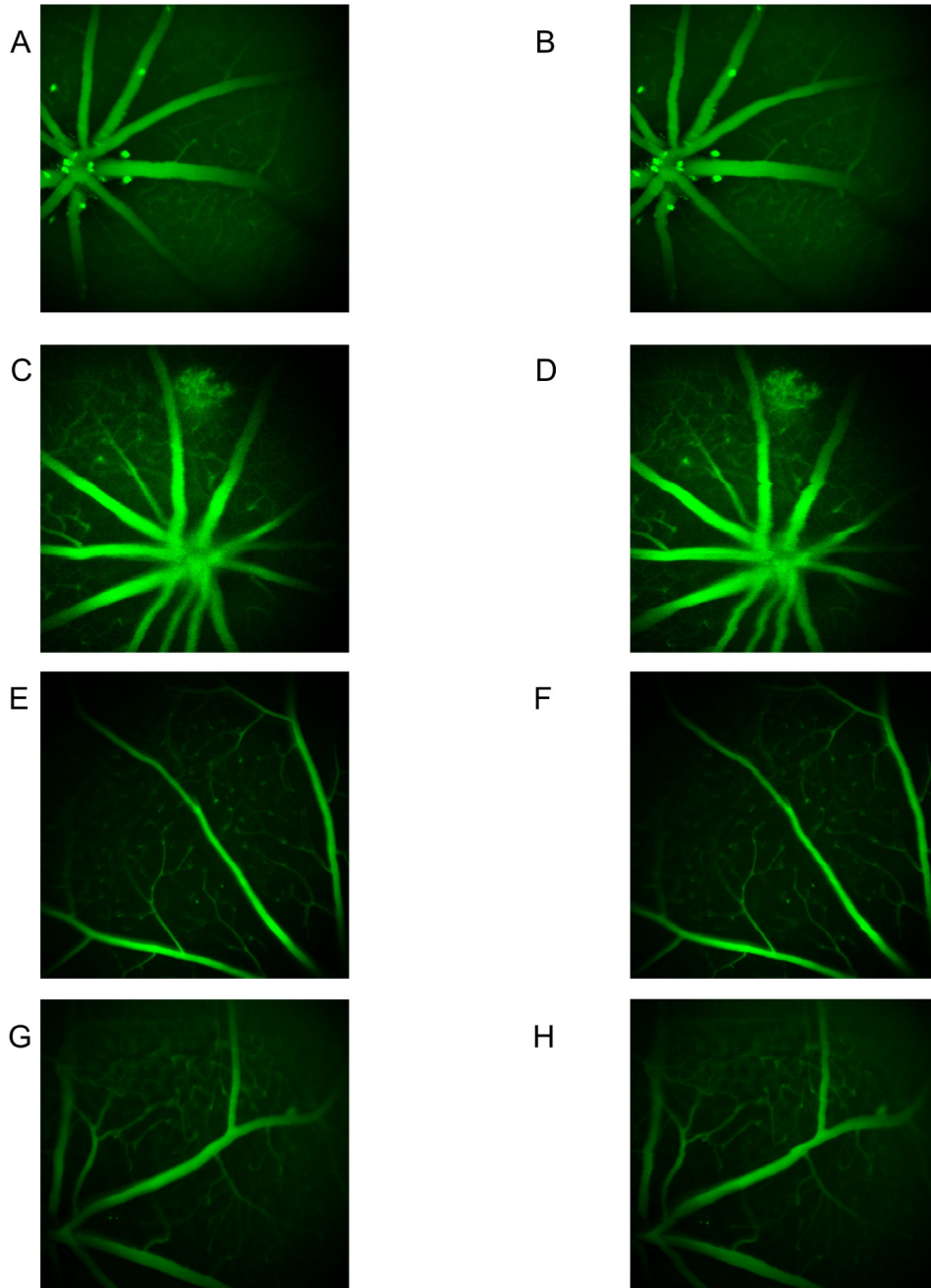


Fig. 7. Average images of capillary fluorescence after injection of fluorescent dye. A, C, E, G) Average images created after images were registered using the unaligned average image as the template. B, D, F, H) Average of collected images using a single manually selected image as the template. A and B included 10 images. C and E included 5 images. E and F included 20 images. G and H included 40 images.

Table 1. Normalized variance of RPE image averages^a under differing registration conditions

Laser power (mW)	Registration								
	None			Template					
			Average			Single-image ^b			Template Δ NV (%) ^d
	NV	SNR	NV	SNR	Δ NV (%) ^c	NV	SNR	Δ NV (%) ^c	
6.2	0.470	89.9	0.479	99.0	1.9	0.476	98.5	1.4	−0.5
3.2	0.415	48.9	0.419	51.9	0.9	0.423	55.1	2.1	1.1
2.1	0.307	41.9	0.308	42.3	0.4	0.316	42.6	2.7	2.3
1.5	0.255	38.4	0.256	39.9	0.4	0.263	40.4	3.4	3.0
1.0	0.267	32.3	0.268	33.3	0.2	0.273	36.2	2.0	1.8

^aAverage of 150 images

^b31 mW

^cPercent change in NV relative to no registration – bold denotes significant change

^dPercent change in NV between Average and Single-image template-based averages – bold denotes significant change

Table 2. Normalized variance of retina vessel image averages under differing registration conditions

Image Set ^w	Num. Images	Registration							
		None		Template					
				Average			Single-image ^x		
		NV	SNR	NV	SNR	Δ NV (%) ^y	NV	SNR	Δ NV (%) ^y
a	9	0.514	256	0.546	256	6.2	0.551	256	7.1
b	5	0.962	256	1.052	256	9.3	1.088	256	13.0
c	20	1.493	256	1.561	256	4.6	1.537	256	3.0
d	40	0.562	221	0.629	200	12.0	0.622	226	10.7

^wCorresponds to the row in Fig. 4 and Fig. 7

^xManually selected

^yPercent change in NV relative to no registration – bold denotes significant change

^zPercent change in NV between Average and Single-image template-based averages – bold denotes significant change

3.3 Registration performance

The ability of the registration algorithm to converge to a satisfactory compensation of motion has previously been defined as obtaining a Pearson correlation between the target and template image of 0.85 or greater [29]. For each data series of RPE and retina vasculature, the Pearson correlation between every template and target was measured, and for each set of images the mean and standard deviation of the Pearson correlation was calculated. Based on having an average Pearson correlation of at least 0.85, registration is successful for image data sets of RPE for laser-powers of 6.2 mW, 3.2 mW, and 2.1 mW (Table 3). Registration was successful for all image data sets of retina capillaries (Table 4).

3.4 Compensated motion magnitudes

If the registration algorithm successfully converges, the optimized parameters can be used to describe the amount of motion that is occurring between the template and target image [29]. Therefore, this analysis was performed to describe the the average displacement between pixels in the template and target image across all images in each data series (Table 3, Table 4).

Table 3. Template to target Pearson correlation and pixel displacement of RPE images^a

Laser power (mW)	Registration Template							
	Average				Single-image ^b			
	Pearson Correlation		Pixel displacement (pixels)		Pearson Correlation		Pixel displacement (pixels)	
	Mean	Std. dev.	Mean	Std. dev.	Mean	Std. dev.	Mean	Std. dev.
6.2	0.95	0.00	1.08	0.57	0.94	0.01	4.50	0.92
3.2	0.88	0.01	0.94	0.42	0.86	0.01	5.24	0.46
2.1	0.87	0.01	0.76	0.44	0.86	0.01	1.57	0.60
1.5	0.83	0.01	0.73	0.41	0.80	0.01	2.73	0.48
1.0	0.80	0.01	0.66	0.44	0.75	0.01	1.99	0.54

^a150 images per series^b31 mW**Table 4. Template to target Pearson correlation and pixel displacement of RPE images^a**

Image Set ^w	Num. Images	Registration Template							
		Average				Single-image ^x			
		Pearson Correlation		Pixel displacement (pixels)		Pearson Correlation		Pixel displacement (pixels)	
		Mean	Std. dev.	Mean	Std. dev.	Mean	Std. dev.	Mean	Std. dev.
a	9	0.99	0.00	2.88	1.52	0.99	0.00	3.54	1.94
b	5	0.98	0.00	5.34	1.19	0.98	0.01	7.21	1.40
c	20	0.99	0.00	1.77	0.46	0.97	0.01	3.44	0.96
d	40	0.98	0.00	2.85	1.49	0.97	0.01	3.75	2.03

^wCorresponds to the row in Fig. 4 and Fig. 7^xManually selected

3.5 Diminishing returns of adding more images to the averaged image

TPM was used to collect 150 images of RPE cells at laser powers of 1.5 mW, and 1.0 mW. Each set of images was averaged together to investigate the effect of the number of images included in the average on the resulting image quality and the amount of improvement in image quality afforded by adding even more images into the average. However, upon averaging images, the intensity range and variance is decreased compared to the individual images, as a result of the smoothing that occurs with averaging. So, NV and SNR values for image averages computed from different numbers of images are difficult to compare. To overcome this and plot the effect of increasing the number of images included in an average image, we normalized the SNR by the NV for the averaged image. By dividing the SNR by the NV, this quantity takes into account the smoothing that occurs upon averaging and allows the quality of average images created with differing number of single images to be compared. This value was plotted versus a varying number of images which are included in the average. Data is shown for images collected with 1.5 mW and 1.0 mW (Fig. 8). Each datapoint shows the mean and standard deviation of five random accumulations from the given image series. For both laser-power levels, as more images were included in the average, the improvement

in image quality decreased and eventually leveled-off (Fig. 8). Very little image quality was gained after including approximately 40 images in the average.

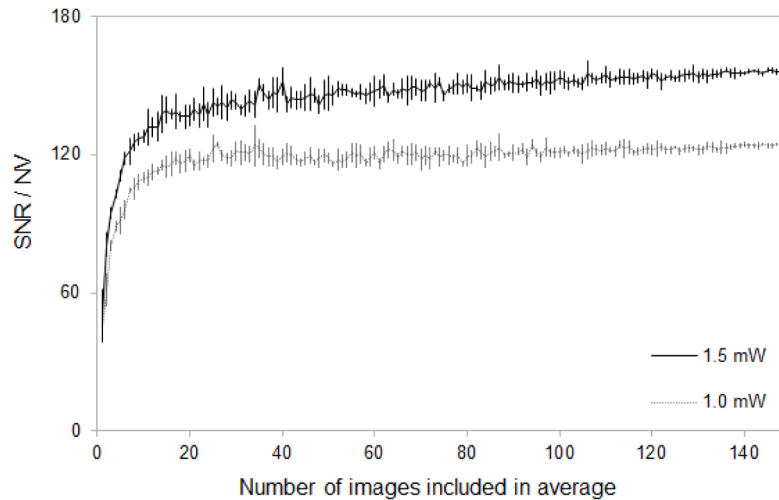


Fig. 8. Image quality as between 1 and 150 images were included in the image average data series collected with 1.5 and 1.0 mW. Image quality is calculated as SNR/NV . Images were registered to the unregistered average image. Vertical bars indicate standard deviations of five random accumulation trials for a given number of images.

4. Discussion

The present work demonstrates the ability to image RPE cells with low laser powers and retina capillaries *in vivo* using two-photon fluorescence microscopy, without reflectance imaging hardware. Previous studies involving *in vivo* two-photon fluorescence imaging of the retina relied upon reflective imaging hardware [21–25, 27, 28]. However, using reflectance imaging requires incorporation of (a) additional light sources which in turn diminish the allowable power of laser light for TPM, and (b) optical components to couple the reflectance imaging light source and detector which complicates the system and can introduce unwanted dispersion. The current work also shows the behavior of the method and resulting data for laser powers ranging from 6.2 mW down to 1.0 mW, and RPE structure is distinguishable in image data collected with 1 mW laser power.

In real-world applications, the option to obtain an ideal or favorable template for image registration at high laser powers is not feasible [14]. For example, in the average image shown in Fig. 7(D), perturbations that were present in the single-image template used for registration are evident by the distortions in the the large vessels. Using a template comprised of the non-registered average reduces but does not eliminate the distortions in the final average image (Fig. 7(C)).

It is important that the collected data contain the information needed to register images without high radiation exposures. To obtain a highly fluorescent individual image of RPE to use as an ideal template for each data series, a single image was collected at 31 mW of laser-power. In contrast, imaging the retina vasculature at the 5 mW laser-power with FITC-BSA injection produces high fluorescence for all images collected, allowing any image in a data series to be used as a template and without the need to collect a separate image at higher laser power. The current results indicate that an ideal template image is not required to improve image quality through averaging after registration. An unregistered average of a set of images can suffice as a template to improve image quality compared to the unregistered average. At laser powers of 3.2 mW and below, registration of images using the unaligned average image as the template does not provide quantitatively significant improvement of the final image

compared to averaging images without registration. However, for images collected of RPE at 6.2 mW and retina capillaries at 5 mW, using the unaligned average as the template provides significant improvement. This includes the instance of the maximum observed displacement of 10 μm . This suggests that such motions do not preclude the use of an unregistered average image as the template, if individual images contain sufficient structural detail. With larger movement amplitudes than observed in the current data sets, using the averaged image as the template could have decreased efficacy. One possible solution to this problem would be an iterative approach wherein the resulting registered averaged image is used as the template for a subsequent round of registration and averaging.

Due to the decreasing levels of signal in the low power two-photon fluorescence images, the performance of the registration algorithm to successfully compensate motion was investigated. It was previously shown that if the algorithm obtains a Pearson correlation between the target and template image of 0.85 or greater, the method can be said to have successfully determined and compensated the motion between images [29]. By this metric, the registration algorithm was successful for all image sets, except for the lowest laser powers of 1.5 mW and 1.0 mW. Interestingly, when using an ideal template for registration, a significant improvement in image quality is achieved compared to averaging the 1.5 mW and 1.0 mW images without registration. This indicates that metrics complementary to the Pearson correlation could be investigated for indicating successful registration. The registration algorithm was able to successfully compensate large motions. It successfully compensated when the average pixel displacement between template and target was 7.2 pixels (13.7 μm). This indicates that observed failures of the algorithm to converge are not due to its ability to compensate large motions, but more likely due to the low signal found in images collected with 1.5 mW and 1.0 mW of laser-power. The amount of motion measured between template and target images was greater when an unregistered average image was used as the template, compared to using a single image.

The present method used for registration was developed and tested for use with two-photon fluorescence imaging, and, specifically, neuronal imaging, although it is a generally applicable method [29]. Previous studies of *in vivo* fluorescence retina imaging [13, 14, 21–25] use a common registration method [26]. However, this method [26] performs best when correcting horizontal distortions and does not handle torsional or rotational distortions [14, 25], because it relies upon maximizing the cross correlation between wide horizontal strips of image. The currently used method [29] can freely compensate in the horizontal and vertical direction within an imaging frame as needed, making it suitable in the presence of both translational and rotational intra-frame distortions. Further, the current method was explicitly tested and demonstrated to be robust under noisy conditions [29], which was especially pertinent to the present study as laser power was reduced.

Due to movements during data collection, image registration provides an improvement in the average image compared to the average of non-registered images. Sources of movement in the present study include heartbeat and breathing. These result in oscillatory motions that are small compared to the image frame. However, the registration method begins by performing a global rigid registration, so translational motion would also be taken into account, if present [29].

The registration algorithm relies upon identifying common features between the template and image of interest. However, as the laser power is reduced to 1.5 and 1.0 mW, the observable features significantly decrease compared to those obtained at higher laser powers. Thus, it was unclear if the lower laser power images would contain sufficient information for the image registration algorithm to make a difference. Our results indicate that even with few qualitatively observable features in individual images (see Fig. 2 and Fig. 3, left-side images), the algorithm can effectively (based on Pearson correlation) register images to a template, and, upon averaging images, biological structures are identifiable which were not so within individual images (compare left- versus right-side images in Fig. 2 and Fig. 3), and significant improvement in average image quality can be achieved (see Table 1, second to last column on the right). These results complement previous work [13, 20–22] in demonstrating the

importance of image registration and averaging to maximize information content derived from an *in vivo* two-photon fluorescence imaging data set.

Signal averaging is a powerful tool for improving the signal-to-noise levels in images. However, as more images are averaged, the improvement in image quality diminishes. Biophysical methods such as cryo-electron microscopy can collect millions of particle images for averaging [45], but unfortunately, this is not possible when imaging live biological specimens. Photobleaching and photodamage are of particular concern when imaging light-sensitive tissues such as the retina [46, 47]. Additionally there are constraints about how long non-anaesthetized subjects can remain stationary. Thus, it is critical to determine the effect of collecting additional images on the amount of information gained. Our results show that in TPM little additional information is gained by collecting more than 40 images for laser powers of 1.5 mW and 1.0 mW. The more rapid decrease in image quality improvement seen with low laser power indicates that features are more masked by noise as compared to images collected at higher-laser power.

The current study focused on the retinal capillaries as well as RPE. Both have been implicated in the development of a number of important retinal diseases. The retinal vasculature has long been recognized as major site of pathology in diabetic retinopathy [48] and AMD [49], whereas RPE has been recognized to play important roles in models of retinal degeneration and with defects in retinoid cycle [1]. In addition, a recent study [50] implicated the RPE also in the development of lesions that are characteristic of diabetic retinopathy. The instrumentation and methodology described in the present work can be used to assess the impact of drugs on these pathologies.

There are no established maximum permissible exposure (MPE) limits for a mouse eye. Considering differences between numerical apertures (NA) of human and mouse eyes, MPEs can be assessed for imaging mouse eye by using ANSI limits established for humans and dividing them by the squared ratio of mouse eye NA to the human eye NA [51]. Thus, mouse MPE are expected to be about 5 times lower than human MPE. Based on these assumptions and imaging conditions with 750 nm excitation, 1mW and 72 s exposure, light levels were 3 times higher than safe estimates based on the scaled ANSI limit for humans.

If two-photon fluorescence imaging will be utilized clinically, the capability to image biological structures with low laser power is essential [13, 15–18]. The current and prior [13, 20–22] work indicate image registration and averaging will be an essential component of deriving images with clinically significant information.

Appendix figures

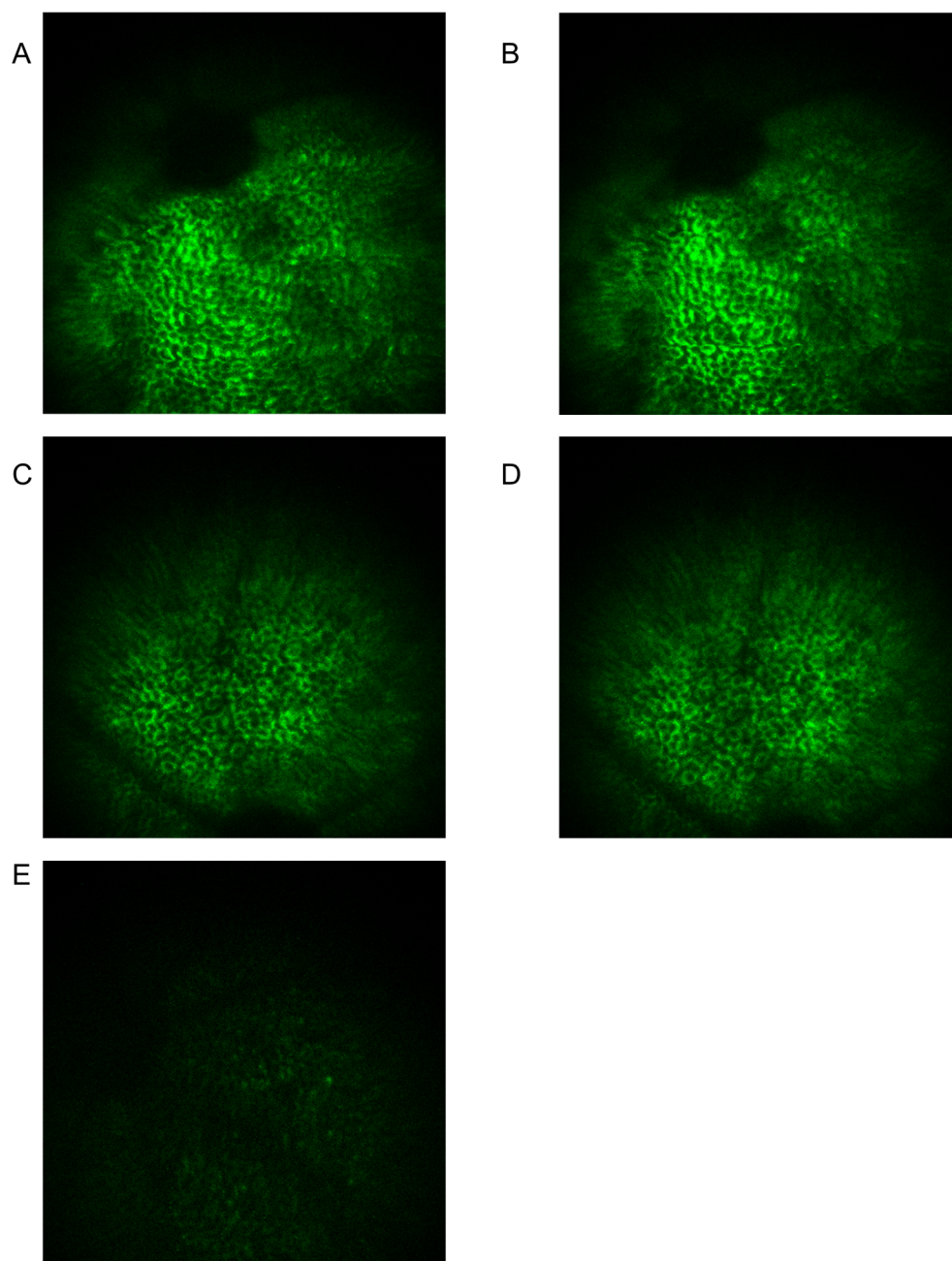


Fig. 9. High laser-power images collected at 31 mW. A, B, C, D, E) correspond with the RPE images collected at 6.2, 3.2, 2.1, 1.5, 1.0 mW, respectively.

Conflict of interest statement

G.P. is an employee of Polgenix, Inc. K.P. is CSO at Polgenix Inc. and an inventor of U.S. Patent No. 7706863 – “Methods for assessing a physiological state of a mammalian retina”,

and U.S. Patent No. 8346345 B2 – “Methods for assessing a physiological state of a mammalian retina” with values that may be affected by this publication.

Author contributions

N.S.A, G.P., and K.P. conceived the project. G.P. and P.S. carried out the imaging experiments. N.S.A developed the software. N.S.A and G.P. wrote the manuscript. N.S.A, G.P., P.S., M.W., T.S.K. and K.P. edited the manuscript.

Acknowledgments

This work was supported by funding from the National Institutes of Health 1K99EY025007 (N.S.A), EY024864 (T.S.K.), EY025451 (K.P.) the Arnold and Mabel Beckman Foundation, and Ohio Third Frontier (State of Ohio) TECG20150049. K.P. is the John H. Hord Professor of Pharmacology. This work was also supported by the TEAM project financed by European Union within the framework of Innovative Economy coordinated by Foundation for Polish Science (P.S. and M.W.).